3B2v8.06a/w (Dec 5 2003).51c XML:ver:5.0.1 YSNMR : 271 Prod.Type:COM pp.1–14(col.fig.:1) ED:Kulkarni PAGN:Kaushik SCAN:Roopa

ARTICLE IN PRESS

Available online at www.sciencedirect.com

SCIENCE DIRECT®

ELSEVIER

Solid State Nuclear Magnetic Resonance ▮ (▮▮▮▮) ▮▮▮–▮▮▮

Solid State Nuclear Magnetic Resonance

www.elsevier.com/locate/ssnmr

Dynamic nuclear polarization and nuclear magnetic resonance in the vicinity of edge states of a 2DES in GaAs quantum wells

Clifford R. Bowers[a,*], Joshua D. Caldwell[b], Guennadi Gusev[c], Alexey E. Kovalev[d], Eugene Olshanetsky[e], John L. Reno[f], Jerry A. Simmons[f], Sergey A. Vitkalov[g]

[a]*Department of Chemistry and the National High Magnetic Field Laboratory, University of Florida, P.O. Box 117200, Gainesville, Florida 32611-7200, USA*
[b]*Naval Research Lab, Power Electronics, 4555 Overlook Ave, S.W., Code 6881, Washington, DC 20375, USA*
[c]*Instituto de Física, Universidade de São Paulo, Caixa Postal 66318, 05315-970, São Paulo, SP, Brasil*
[d]*Department of Electrical Engineering, Pennsylvania State University, State College, PA, USA*
[e]*Institute of Semiconductor Physics, Novisibirsk, Russia*
[f]*Sandia National Laboratories, MS 1415, Albuquerque, NM 87185, USA*
[g]*City College of New York at CUNY, Physics Department J-419, Convent Avenue at 138th Street, New York, NY 10031, USA*

Received 5 July 2005

Abstract

Nuclear magnetic resonance is detected via the in-plane conductivity of a two-dimensional electron system at unity Landau level filling factor in the regime of the quantum Hall effect in narrow and wide quantum wells. The NMR is spatially selective to nuclei with a coupling to electrons in the current carrying edge states at the perimeter of the 2DES. Interpretation of the electron-nuclear double resonance signals is facilitated by numerical simulations. A new RF swept method for conductivity-detected NMR is introduced which offers more efficient signal averaging. The method is applied to the study of electric quadrupole interactions, weakly allowed overtone transitions, and evaluation of the extent of electron wave function delocalization in the wide quantum well.

Keywords: Quantum well; Parabolic Quantum well; ENDOR; Two-dimensional electron system; Quantum Hall effect; GaAs; DNP; Fictitious spin-1/2; Overtone transitions

1. Introduction

Recent interest in spin-based electronics and quantum computing has stimulated numerous experimental and theoretical studies of spin-related phenomena in solid-state semiconductor nanostructures. Magnetic resonance spectroscopy is the ideal tool for evaluating spin interactions, spin-lattice relaxation times and coherence dephasing mechanisms in potential candidate materials for spin-based device applications. Transport detection of magnetic resonance affords several key advantages over conventional resonant cavity or tuned coil methods in quantum confined semiconductors. Most importantly, the limited number of electron or nuclear spins in a nanostructure such as a single quantum dot or quantum well (QW) presents a challenge to the sensitivity of tuned coil or bridge techniques. The inefficiency of detecting MHz or GHz frequency photons is not relevant to optical or charge transport-based detection. Transport detection provides direct access to the spin Hamiltonian and spin relaxation mechanisms relevant to the operation of spin-based devices because the spectroscopy is selective to the conduction channel. Information pertaining to defects [1,2], tunneling [3], and symmetry breaking interactions, which can produce electric quadrupole splittings in NMR [1,4–10] and electron g-factor anisotropy [11–14], can be obtained. Nuclear spin relaxation is found to be extremely sensitive to Landau Level filling [14–16]. The Knight shift [17,18] (i.e. the shift of the nuclear spin Larmor frequency due to coupling to the polarized conduction electron system) can be used to map the electronic wavefunction [19,20] and to

*Corresponding author. Fax: +1 352 392 8758.
E-mail address: cliff.bowers@gmail.com (C.R. Bowers).

0926-2040/$ - see front matter © 2005 Published by Elsevier Inc.
doi:10.1016/j.ssnmr.2005.08.011

study spin depolarizing many-body excitations in the quantum Hall effect (QHE) [10,21–25].

Beyond spectroscopic characterization of internal Hamiltonians and relaxation mechanisms, quantum information processing requires (a) preparation of the density operator in a pure state and (b) preparation and detection of entangled quantum states [26,27]. Methods for the manipulation of spin Hamiltonians using RF fields and/or sample rotation, which date back to the spin-echo [28], magic angle spinning [29], and multiple pulse NMR [30], have become increasingly sophisticated over the past 30 years [31,32]. Thus, it is not surprising that some of the first demonstrations of elementary bit operations and entanglement were performed in molecular spin systems [33]. However, molecular systems suffer at least two limitations that are obviated in semiconductor nanostructures: the ability to prepare the system in a pure state of and the need for integration with conventional semiconductor electronics. The demonstration of g-factor control in a QW using an external gate [34,35] represents one of the first examples of such integration.

Conductivity-detected magnetic resonance spectroscopy is uniquely suited to studies correlating spin interactions with transport properties of a 2DES [15,25,36]. In magnetoresistivity-detected electron-nuclear double resonance (MDENDOR), NMR spectra are selective to nuclei with an appreciable hyperfine contact interaction to electrons in the path of the source-drain current. At odd-integer filling factors in the regime of the QHE, the MDENDOR spectrum is spatially selective to nuclei with a coupling to electrons in the current carrying edge states which occur within a few magnetic lengths l_0 of the perimeter of the 2DES [37,38].

Here, the in-plane longitudinal magnetoresistance ΔR_{xx} of a 2DES at unity Landau level filling factor in the regime of the QHE is used as the detection channel for ESR and NMR transitions in two different types of remotely n-doped, high electron mobility quantum structures: a superlattice consisting of 20 individual 30-nm-wide square QWs (sample EA124) and a 400-nm-wide GaAs/AlAs digital parabolic QW (sample AG662). It is already well-established that in such structures the nuclear field B_n associated with the electron-nuclear Fermi contact interaction can be enhanced by dynamic nuclear polarization (DNP) [17,18]. The induced nuclear field, in turn, shifts the ESR condition. Consequently, the ESR may become "pinned" to the external field [15,39–41]. NMR is detected via the change in resonant microwave absorption due to perturbation of B_n.

This paper is organized as follows. First, we investigate the effect of increasing B_n on the MDENDOR spectra. The changes are dramatic, but can be interpreted by a simple physical explanation. The hypothesis is confirmed by numerical simulations based on a model for DNP that will be presented. The field swept ^{75}As MDENDOR spectrum acquired at small initial B_n exhibits three resonances. Expression of the spin Hamiltonian and density operators in terms of fictitious spin-1/2 operators permits the change in nuclear field due to selective CW-NMR irradiation of individual satellite and central transitions to be calculated and compared to experiment. These results provide the impetus for the proposal and demonstration of a new RF swept ENDOR technique which facilitates more efficient signal averaging and allows spectra to be acquired at constant applied magnetic field and hence constant Landau level filling factor. The new technique will be demonstrated with (i) a study of electric quadrupole interactions in EA124 and AG662, (ii) observation of weakly allowed overtone transitions of nuclei situated in the conduction channel and (iii) evaluation of the extent of electron wave function delocalization in a wide PQW.

1.1. Quantum wells, energy spectrum of a 2DES, and transport properties

A QW is a conduction band potential energy well formed by sandwiching a relatively low band gap semiconductor between broad barriers of a higher band gap semiconductor. For studies requiring ultra-high electron mobility, the $Al_xGa_{1-x}As/GaAs/Al_xGa_{1-x}As$ structure (where typically $x = 0.1 \rightarrow 0.4$) has the advantage of nearly perfect lattice matching between the barrier and well layers, yielding interfaces which are nominally unstrained and free of defects. QWs can be grown by various methods, but the highest electron mobilities (c.a. $\approx 30 \times 10^6\,\Omega/\mathrm{cm}^2$) have been achieved by molecular beam epitaxy. To obtain a 2DES in a QW, electrons are introduced by remote silicon δ-doping, where a sub-monolayer of Si is deposited inside the $Al_xGa_{1-x}As$ barriers. Remote doping eliminates the scattering (and hence increases the mobility) that would result if the Si were deposited directly into the well layer. After cooling to a few degrees Kelvin, a red LED placed near the sample is switched on for a few tens of seconds to ionize the Si donors, resulting in increased 2D density and channel mobility.

At zero field, electrons in a QW move freely in the $x-y$ plane, but their translation along z is quantized into electric subbands. In a square potential well of width W_e, the energy spectrum is given by

$$E_i = \frac{\hbar^2}{2m}(k_x^2 + k_y^2) + \frac{(i\pi\hbar)^2}{2mW_e^2}, \tag{1}$$

where i is the subband quantum number and m is the effective mass. Application of a magnetic field along z confines the motion in the $x-y$ plane to cyclotron orbits, yielding a series of Landau levels for each subband:

$$E_{i,n} = E_i + \hbar\omega_c(n + 1/2), \quad \text{where } n = 0, 1, 2, \ldots, \tag{2}$$

$\omega_c = eB_\perp/m$ is the cyclotron frequency, $B_\perp = B_0 \cos\theta$ and θ is the angle between z and Z, the direction of the applied magnetic field, B_0. The Landau levels have a degeneracy proportional to $B_\perp$. At high field and low temperature, where $\omega_c\tau \gg 1$ (τ is the scattering time), the

energy spectrum becomes resolved, and the occupancy of the spin-split Landau levels can be characterized by a filling factor ν, the ratio of the 2D electron density to the spin-split Landau level degeneracy per unit area. A filling factor $\nu = 1$ signifies that the lower energy spin state of the $n = 0$ Landau level is filled exactly. The exchange-enhanced spin splitting $\Delta E_{spin} = g * \mu B_0$ can be decomposed into contributions from the bare Zeeman energy $g\mu_B B_0$ and an exchange-correlation term [42,43]:

$$\Delta E_{spin} = \Delta E_{ex}(B_\perp) + g\mu_B B_0. \quad (3)$$

In the presence of the perpendicular field, the surface conductivity and resistivity are 2×2 tensors satisfying $\tilde{\sigma} \cdot \tilde{\rho} = \tilde{1}$. The elements of $\tilde{\sigma}$ can be obtained experimentally from resistance measurements on the Hall bar. A dc current I_x is forced to flow between the source and drain. At high magnetic field, where $\omega_c \tau \gg 1$, $\sigma_{xy} = I_x V_H = 1/\rho_{xy}$, and

$$\sigma_{xx} = \sigma_{yy} = \frac{\rho_{xx}}{\rho_{xx}^2 + \rho_{xy}^2}. \quad (4)$$

In an ideal 2DES, Landau levels occur at discrete energies $\hbar\omega_c(n + 1/2)$, but disorder and phonon scattering broadens the levels in real samples, yielding localized states within the energy gap. When the Fermi energy E_F falls in the localized states within the gap, integer filling factors are obtained and V_H becomes field independent. The Hall conductivity σ_{xy} is quantized in integer multiples of e^2/h [44]. A simple physical explanation for the vanishing longitudinal conductivity ($\sigma_{xx} \to 0$) is that there are no thermally accessible unoccupied states into which the electrons can scatter. The absence of current dissipation thus leads to a vanishing longitudinal resistivity, and according to Eq. (4), $\sigma_{xx} \propto \rho_{xx}$ as $\rho_{xx} \to 0$.

In an ideal 2DES, the current would be homogeneous over the channel width, L_y. In real systems, however, where band-bending produces edge states, the current flow is localized to regions within a few magnetic lengths ($l_0 = \sqrt{\hbar/eB} \approx 15\,\text{nm}$ at 5 T) of the perimeter of the Hall bar, where E_F intersects the edge-perturbed Landau levels, as illustrated in Fig. 1b. Thus, the observed magnetic resonance signals will reflect the spin interactions in this region. This situation is unlike that of optically pumped NMR which probes nuclei primarily in the bulk 2DES.

If the discussion is restricted to odd-integer filling factors, where the Fermi energy falls in the energy gap ΔE_{spin} separating spin-up and spin-down states of the same Landau level, thermal activation of $R_{xx} = L_x \rho_{xx}$ provides a method for measuring ΔE_{spin} [42,43]. Thus, $R_{xx} = R_0 \exp(-\Delta E_{spin}/2kT)$. However, the exchange enhanced spin-splitting ΔE_{spin} observed by thermal activation of transport is not the same spin splitting observed by ESR, which in accordance with Kohn's theorem, probes the bare g-factor associated with the $k = 0$ excitations. The process by which absorption of a microwave photon of energy $g\mu_B B_0$ yields an excitation with energy ΔE_{spin} has been explained previously in terms of a resonant heating effect

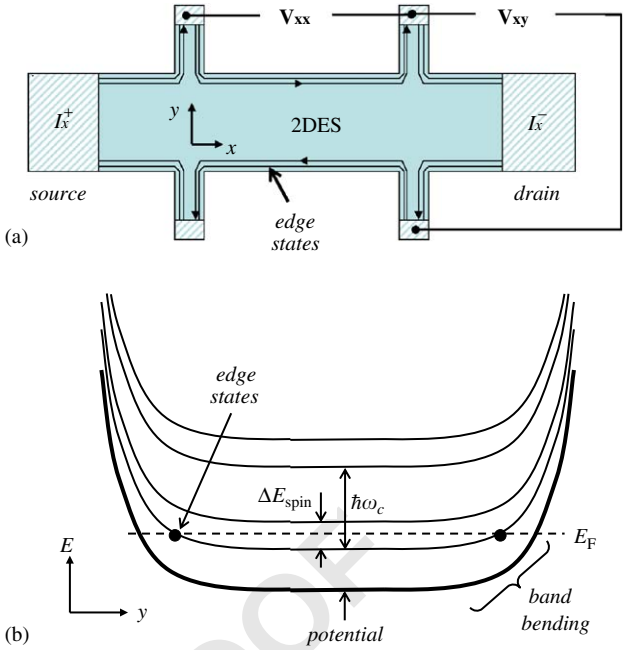

Fig. 1. (a) Schematic of a Hall bar showing the arrangement of electrical contacts to the 2DES and the path of the edge currents. (b) Energy spectrum of the 2DES illustrating the formation of edge states due to band bending of Landau levels.

[45]. This mechanism is adopted in the simulations described below.

1.2. Dynamic nuclear polarization model

The dynamics of the nuclear spin Zeeman order $\langle \hat{I}_z \rangle(t, z)$ on each spin-bearing isotope in the vicinity of a 2DES is described by the following partial differential equation [18,45]:

$$\frac{\partial \langle \hat{I}_z \rangle}{\partial t} = -\frac{1}{T_{1n}(z)}(\langle \hat{I}_z \rangle - \langle \hat{I}_z \rangle_{eq}) - \frac{1}{T_{1n}(z)} \frac{\gamma_e}{\gamma_n} s \langle \hat{I}_z \rangle_{eq} + D \frac{\partial^2}{\partial z^2} \langle \hat{I}_z \rangle - 2W \langle \hat{I}_z \rangle, \quad (5)$$

where

$$s = \frac{\langle S_z \rangle - \langle S_z \rangle_{eq}}{\langle S_z \rangle_{eq}} \quad (6)$$

is the electron spin saturation [18], D is the spin diffusion constant, T_{1n} is the spin-lattice relaxation time, and $2W\langle \hat{I}_z \rangle$ is the spin depolarization rate due to NMR. In DNP, the electron spin Zeeman order $\langle S_z \rangle$ is driven from thermal equilibrium, enhancing the nuclear spin polarization on the time-scale of T_{1n} via cross-relaxation induced by the flip-flop terms in the Fermi contact hyperfine interaction. The same time-constant governs the nuclear spin-lattice relaxation back to thermal equilibrium in the absence of the resonant microwave field. The local nuclear hyperfine field associated with the enhanced Zeeman order on each isotope within the QW of width W_e can be expressed as

$$B_n = b_n \int_{-W_e/2}^{W_e/2} \langle \hat{I}_z \rangle \phi^2(z)\, dz, \quad (7)$$

where b_n is the hyperfine coupling constant of the given isotope and $\phi(z)$ is the envelope factor of the wave function $\psi(z) = \phi(z)u(z)$ in the z-direction ($u(z)$ is the Bloch function). The total nuclear field experienced by the electrons is the sum of the fields due to each isotope: $B_n^{tot} = B_n^{75} + B_n^{69} + B_n^{71}$. Due to the relative signs of γ_e and γ_n for ^{69}Ga, ^{71}Ga and ^{75}As (as well as ^{27}Al), B_n adds constructively to the applied field B_0, yielding the modified resonance condition $h\nu_e = g\mu_B(B_0 + B_n^{tot})$. In the 2DES, DNP induces an enhancement of the local nuclear field which in turn reduces the electron spin saturation until a steady-state is reached. A further increase in nuclear polarization requires increasing s. This may be achieved by slightly reducing the applied magnetic field, which brings the electron spin Larmor frequency closer to resonance with the microwave field. The resulting increased saturation leads to a further increase in $\langle \hat{I}_z \rangle$ until a new steady-state is reached. In practice, a sufficiently slow magnetic field down sweep starting on the high-field side of the resonance line while applying the CW microwave field will produce a continuous increase in B_n^{tot}, thereby "pinning" the ESR to the applied field [15,40,41]. However, if the field sweep is too rapid (i.e. $dB_0/dt > -dB_n^{tot}/dt$), the pinning condition will not be sustained. The maximum B_n^{tot} that can be induced also depends on the available microwave power and the width of the filling factor minimum. At even integer filling factors, $\langle S_z \rangle_{eq} = 0$, so DNP cannot occur.

Spin diffusion is incorporated into the numerical simulations by deriving the following difference formula for the nuclear spin diffusion term (see Appendix A). For a small enough time increment Δt satisfying $2D\Delta t \ll a_0^2$, the change in Zeeman order of nuclei located on the lattice plane at a displacement z from the centre of the QW is described by

$$\Delta\langle \hat{I}_z \rangle(z) = \frac{D}{a_0^2}(\langle \hat{I}_z \rangle(z - a_0) + \langle \hat{I}_z \rangle(z + a_0) - 2\langle \hat{I}_z \rangle(z))\,\Delta t, \quad (8)$$

where a_0 is the lattice plane spacing and D is the spin diffusion constant.

2. Materials and methods

Experimental results will be presented for two types of QW structures. Sample EA124 is a GaAs/$Al_{0.1}Ga_{0.9}$As superlattice consisting of 21 300-Å-wide GaAs QWs separated by 3600 Å $Al_{0.1}Ga_{0.9}$As barriers with a remote Si δ-doping layer located near the centre of each barrier. The mobility and density of this sample is $0.44 \times 10^6\,cm^2/V\,s$ and $6.9 \times 10^{10}/cm^2$ per layer, respectively. This same sample was the subject of previous ESR, ENDOR and optically pumped NMR studies [9,36,41,45]. Sample AG662 is a 400-nm-wide AlAs/GaAs digital PQW, where the average Al mole fraction is zero at the centre and 0.29 at the outer edges. The barriers consist of undoped $Al_{0.31}Ga_{0.69}$As layers. Electrons are introduced by remote silicon δ-doping. A detailed experimental and theoretical analysis of the transport properties in this particular sample has been published [46]. The density and mobility prior to optical illumination with an LED were measured to be $1.5 \times 10^{11}/cm^2$ and $1.2 \times 10^5\,cm^2/V\,s$, respectively. Illumination at ~1.6 K for 60 s by an LED placed 1 cm away increased these values to $3.5 \times 10^{11}/cm^2$ and $2.4 \times 10^5\,cm^2/V\,s$. The activation energy at $\nu = 1$ in the PQW was found to be $\Delta E = 1.9 \pm 0.1$ K in a perpendicular field of 5 T. Seven electric subbands are occupied at zero field, but only the lowest subband is occupied at the high field employed in the present study. The growth direction in both samples is $\langle 1\,0\,0 \rangle$. To facilitate conductivity measurements the 2DES is patterned lithographically into the shape of a Hall bar, as shown in Fig. 1a.

Experiments were performed in an Oxford Instruments superconducting magnet with a 38 mm cold bore, permanently fixed current leads, and a field homogeneity of 100 ppm over a 1 cm diameter spherical volume. The superconducting shim coils on this magnet were not used. The magnet is equipped with an Oxford Heliox ^{3}He top-loading cryostat insert with a 25 mm sample space. The stock probe was modified with the installation of a rotation stage and two stainless steel semi-rigid coaxial cables to facilitate simultaneous RF and microwave irradiation. Each sample was mounted onto a standard non-magnetic 8 pin IC plug. The IC socket is fixed to a rotation stage permitting rotation from $\theta_y = 0 \rightarrow 90^\circ$ about the y-axis of the Hall bar. The x-axis of the sample is the direction of the source-drain current I_x, while the z-axis is the growth direction. The ESR spectrum is acquired by sweeping B_0 at fixed microwave frequency while recording the microwave induced ΔV_{xx} signal. To improve the S:N and to remove the rectification signal, a double lockin scheme is used wherein both the source-drain current and microwave field are amplitude modulated. The RF field for excitation of NMR was generated by a ~5-mm-diameter planar coil adjacent to the sample. The longitudinal resistance change is derived from $\Delta R_{xx} = \Delta V_{xx}/I_x$. A 10 MΩ resistor is placed in series with the source-drain resistance to ensure a constant current through the sample. All experiments were performed with $I_x < 1\,\mu A$ unless otherwise specified. Additional details about the experimental setup, data acquisition parameters and the microwave system are given elsewhere [36,45].

3. Results and discussion

3.1. Magnetoresistively detected electron-nuclear double resonance

The possibility to exploit the pinning effect for detection of NMR is well known [15,39,41]. The NMR excitation

produces a perturbation of the pinning condition which results in a sudden increase in the resonant microwave absorption. The change in the nuclear field due to NMR of a specified isotope will be denoted δB_n. The change ΔR_{xx} due to NMR excitation evolves from a peak to a step-shaped response when the change δB_n is varied from $|\delta B_n| < \delta_{1/2}$ to $|\delta B_n| > \delta_{1/2}$, where $\delta 1/2$ is the ESR line width. This effect is demonstrated in the series of ^{71}Ga MDENDOR spectra shown in Fig. 2 recorded at varying RF frequency and constant microwave frequency. When the NMR resonance is encountered at relatively small B_n, as in trace (a), the NMR is manifested as a small absorption peak. As the RF frequency is reduced (traces b, c), the amplitude of the sharp peak increases, but ΔR_{xx} still returns to its pre-NMR value, indicating a return to the pinning condition following the perturbation. As the frequency is reduced further (traces d–f), the increasingly sharp peak is followed by a large downward step. In these traces, ΔR_{xx} returns to the non-resonant value following NMR, indicating that the pinning condition has been permanently lost. A qualitative interpretation for these observations is as follows. When $|\delta B_n| < \delta_{1/2}$, ΔR_{xx} initially increases due to the increased heating resulting from the shift of the ESR toward the resonance position. However, the increase in ΔR_{xx} is transient because the increased absorption also increases the ESR saturation (Eq. (6)), thereby increasing the nuclear spin polarization rate. Thus, B_n returns to its pre-NMR value, and the ESR pinning condition is re-established. On the other hand, if the change induced exceeds the line width (i.e. $|\delta B_n| > \delta_{1/2}$), the ESR absorption line is swept rapidly all the way through to the far side of the resonance condition, and a very sharp peak in ΔR_{xx} is registered. The width of this peak is substantially narrower than the actual NMR absorption line, and in these spectra is limited only by the lockin time constant. The loss of the ESR pinning condition is irreversible, and ΔR_{xx} assumes its non-resonant value. Numerical simulations based on Eqs. (5) and (7) are compared to the data in Fig. 2. The evolution from a peak to a step-shaped NMR response, and the intensity pattern of the MDENDOR peak, are nicely reproduced. The simulations confirm the qualitative explanation of the data.

3.2. Analysis of quadrupole splittings in ^{75}As MDENDOR

The high-field Hamiltonian of a spin $I > 1/2$ nucleus in the rotating frame includes the interaction of the electric quadrupole moment with the electric field gradient (EFG) at the origin:

$$\hat{H}_{int} = \hat{H}_Z + \hat{H}_Q = -\Delta\omega \hat{I}_z + \frac{\omega_Q}{3}[3\hat{I}_z^2 - I(I+1)], \qquad (9)$$

where

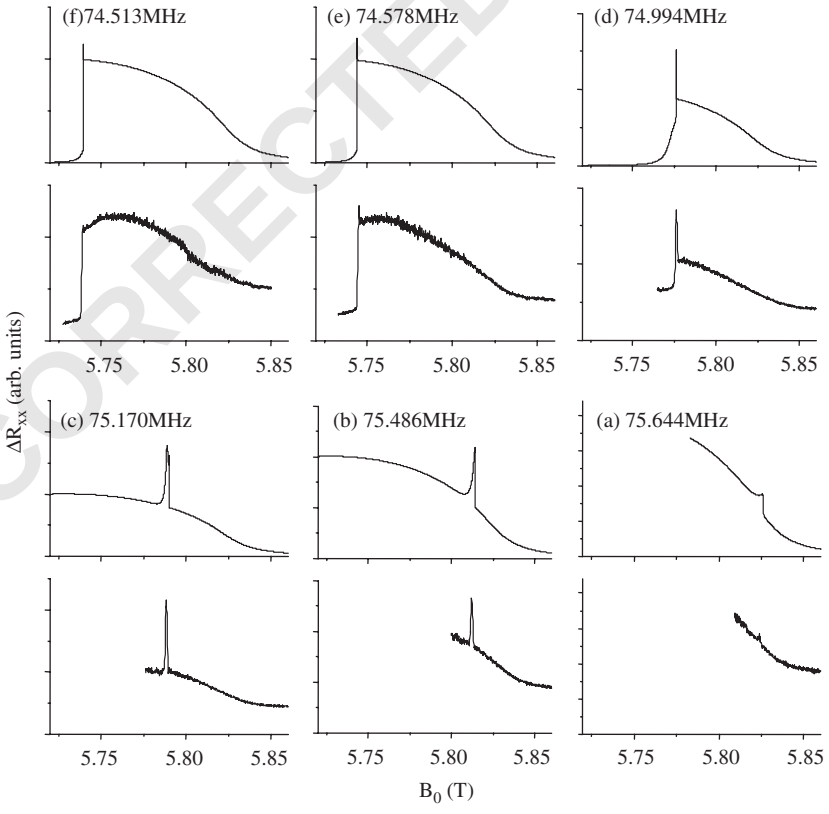

Fig. 2. Comparison of the ^{71}Ga MDENDOR spectra recorded at 1.5 K at a series of fixed RF frequencies (bottom) with numerical simulations (top) based on the model described in the text. The spectra were recorded at a magnetic field down sweep rate of 4.6 mT/min and with a CW microwave frequency of 34.249 GHz.

$$\omega_Q = \frac{3e^2Q}{4I(2I-1)\hbar} \tag{10}$$

is the quadrupole coupling constant, eq represents the field gradient component V_{zz}, and $\eta = (V_{xx} - V_{yy})/V_{zz}$ is the asymmetry parameter, expressed in terms of the principal values of the EFG tensor. Non-secular terms have been neglected. When the principal axis system $(x',y',z',)$ and laboratory axis system $(X,Y,Z,$ where $Z \| B_0)$ are not coincident, the orientation dependence of ω_Q has the form

$$\omega_Q(\theta,\phi) = \omega_Q^0[\tfrac{1}{2}(3\cos^2\theta - 1) + \tfrac{1}{2}\eta\sin^2\theta\cos 2\varphi]. \tag{11}$$

The energy spectrum of the spin $I = \frac{3}{2}$ yields three $\Delta m_I = +1$ transitions, observed at $\Delta\omega = +\omega_Q$, 0 and $-\omega_Q$.

Optically detected and optically pumped NMR studies have shown that quadrupole splittings in GaAs may be induced by strain or internal electric fields [1,4–9]. In one recent report, the ^{75}As quadrupole splitting was used to probe the propagation of sample mounting strain and internal electric fields due to a Schottky barrier near GaAs QWs [4]. In general, quadrupole splittings result when there is a loss of inversion symmetry of the charge distribution about the nucleus. In $Al_xGa_{1-x}As$ alloys, the difference in the Pauling electronegativity of Al and Ga can also produce a non-vanishing EFG at the As sites [1]. As shown in Fig. 3, a $\omega_Q = 55$ kHz quadrupole splitting of the ^{75}As resonance in GaAs QWs is observed by optically pumped NMR on an unpatterned sample of EA124 subjected to a planar stress [9]. In this sample, the GaAs substrate was removed by chemical etching, and the MBE film was epoxy bonded to a thick silicon support. As a consequence of the difference in the thermal expansion coefficients of Si and GaAs, a uniform planar stress in the $x-y$ plane arises upon cooling the sample from room temperature to a few degrees Kelvin. The splitting follows the $\omega_Q(\theta) \propto 3\cos^2\theta - 1$ dependence (see Fig. 4) characteristic of an $\eta = 0$ EFG with $z' \| z$, the MBE growth direction.

The field swept ^{75}As MDENDOR spectrum of EA124 shown in Fig. 5a also exhibits three lines. The splitting and line intensities are similar to those obtained by optically pumped FT-NMR following a short, non-selective pulse. The satellite ($|+1/2\rangle \rightarrow |+3/2\rangle$, $|-3/2\rangle \rightarrow |-1/2\rangle$) and central ($|-1/2\rangle \rightarrow |+1/2\rangle$) transitions are resolved on ^{75}As, but not for ^{69}Ga and ^{71}Ga which have smaller nuclear quadrupole moments by factors of 2.6 and 1.7, respectively. Clearly, each NMR transition in the MDENDOR spectrum of Fig. 5a is associated with a perturbation of the local nuclear field. In a 2DES, where confinement is in the z-direction, the nuclear field associated with the ensemble of nuclei residing on a plane at a specified displacement z is given by $B_n = b_n\langle\hat{I}_z\rangle(z)|\phi(z)|^2$, where $\langle\hat{I}_z\rangle(z) = Tr(\hat{\rho}(z)\cdot\hat{I}_z)$ and $\hat{\rho}(z)$ is the density operator. The density operator at thermal equilibrium is given by $\hat{\rho}_{eq} = Z^{-1}\exp(-\beta_{eq}\hat{H}_{int})$ where $Z = Tr\{\exp(-\beta_{eq}\hat{H}_{int})\}$ and $\beta_{eq} = \hbar/k_B T_{eq}$. Experiments performed at a few Kelvin warrant application of the high temperature approximation, $\hat{\rho}_0 \approx 4^{-1}(1 + \beta_{eq}\omega_0\hat{I}_z)$. In DNP, the spin temperature

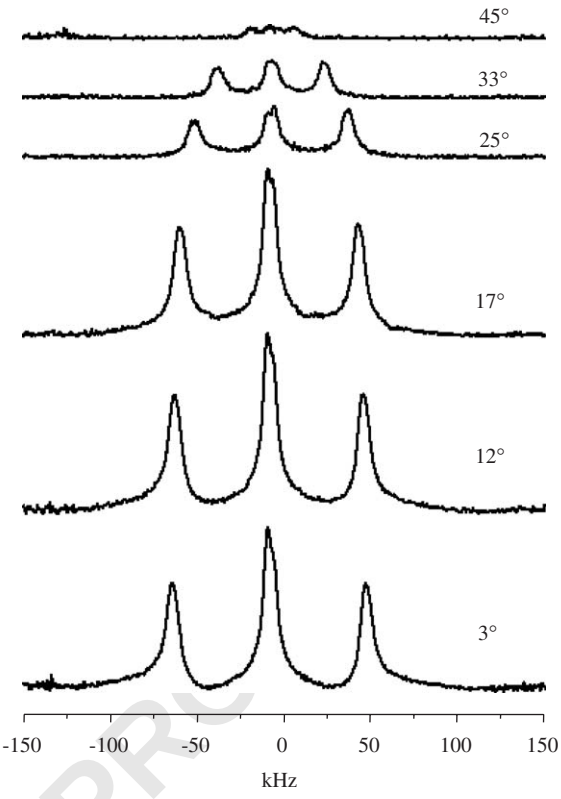

Fig. 3. Optically pumped Fourier transform NMR magnitude spectra of sample EA124 subjected to a planar stress due to thermal contraction, as described in the text. The NMR signals were acquired by ordinary inductive detection at 4.2 K following 60 s of optical pumping with a $\lambda \approx 812$ nm beam with an intensity ≈ 500 mW/cm^2. A single 1 μs RF pulse with a flip angle of 90° was applied to stimulate the free induction decay. The spectra were recorded as a function of the rotation angle with respect to the B_0 field. A summary of the rotation angle dependence of the quadrupole splitting is plotted in Fig. 4.

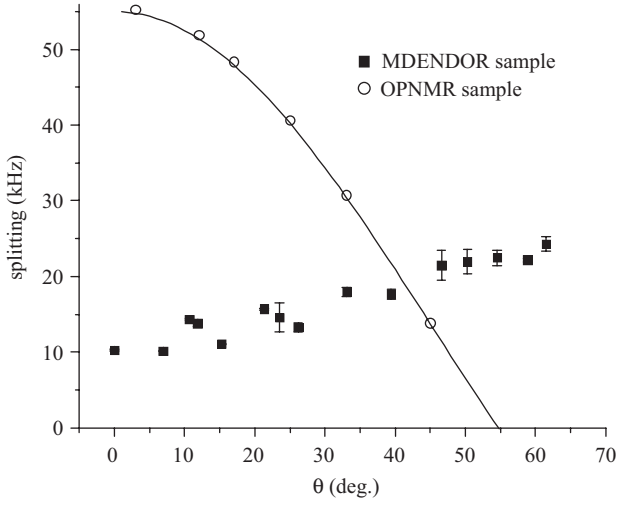

Fig. 4. Tilt angle dependence of the ^{75}As line splitting in EA124 at 1.5 K. The MDENDOR spectra were all acquired at $\nu = 1$. Thus, the resonant condition occurs at higher frequency/field as the tilt angle was increased. The splittings observed by OPNMR on a strained sample of EA124 correspond to the series of spectra presented in Fig. 4. The solid curve represents the function $27.5(3\cos^2\theta - 1)$ kHz.

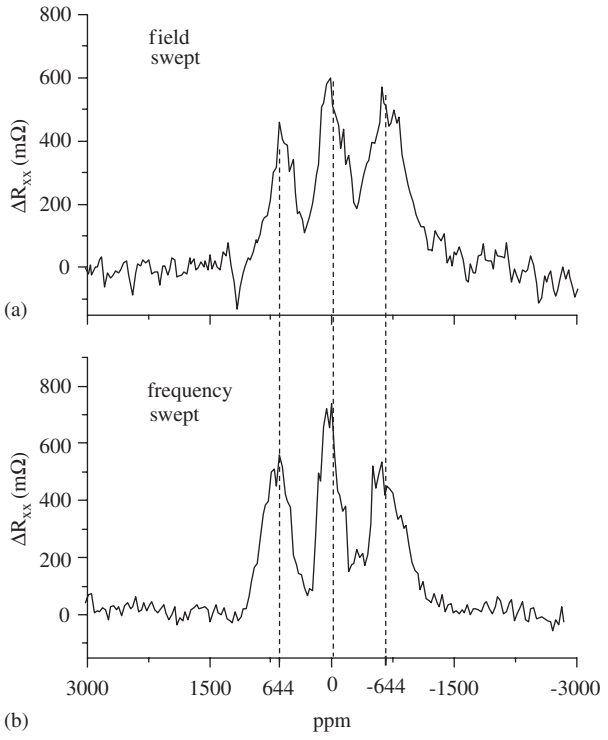

Fig. 5. ^{75}As MDENDOR spectra of EA124 recorded in the vicinity of $\nu = 1$ by two different methods. In each case, the sample was tilted by $\theta_y = 42 \pm 1^\circ$ with respect to the B_0 field. The abscissas of the spectra were converted to ppm with respect to the field/frequency to facilitate direct comparison of the splittings. (a) Spectrum recorded with a field sweep about $B_0 = 3.99\,T$ and a microwave frequency of 24.3 GHz. (b) Spectrum recorded with a frequency sweep about 29.52 MHz with a microwave frequency of 29.1 GHz. The RF frequency was swept from 29.4 to 29.6 MHz at a rate of 1 kHz/s.

is reduced, but for spin polarizations corresponding to nuclear fields in the range relevant to the present work, the high temperature approximation is still valid. Thus, the initial density operator under conditions of steady-state DNP is taken to be $\hat{\rho}_0(z) \approx 4^{-1}(1 + \beta_0(z)\omega_0\hat{I}_z)$, where the spin temperature is now z-dependent. The Zeeman order is computed from

$$\langle \hat{I}_z \rangle = \tfrac{1}{4} Tr((1 + \beta_0\omega_0\hat{I}_z)\cdot\hat{I}_z) = \tfrac{1}{4}\beta_0\omega_0\, Tr(\cdot\hat{I}_z^2) = \tfrac{5}{4}\beta_0\omega_0. \quad (12)$$

The change in the nuclear field due to selective CW irradiation of each single quantum transition can be derived using the fictitious spin-1/2 operator formalism introduced by Pines and Vega [47,48]. The total Hamiltonian including the interaction with an RF field applied along the rotating frame x-axis is $\hat{H}_1 = -\omega_1\hat{I}_x$, yielding

$$\hat{H} = \hat{H}_{int} + \hat{H}_1 = -\Delta\omega\hat{I}_z + \frac{\omega_Q^0}{3}[3\hat{I}_z^2 - I(I+1)] - \omega_1\hat{I}_x \quad (13)$$

The time evolution obeys

$$\frac{\mathrm{d}}{\mathrm{d}t}\hat{\rho}(t) = -i[\hat{H},\hat{\rho}] - \frac{\hat{\rho}_{off}}{T_2} - \frac{\hat{\rho}_{diag} - \hat{\rho}_0}{T_1}, \quad (14)$$

where $\hat{\rho}_{off}$ and $\hat{\rho}_{diag}$ are the off-diagonal and diagonal components of the density operator (expressed in the eigenbasis of $\hat{H}$), respectively, and T_1 and T_2 are the spin relaxation times which are taken to be equal among all populations and coherences, respectively. Analytical solution of Eq. (14) is facilitated by expressing both the Hamiltonian and density operator in the fictitious spin-1/2 operator basis [48]:

$$\hat{H} = -\Delta\omega(3\hat{I}_z^{1-4} + \hat{I}_z^{2-3}) + \omega_Q(\hat{I}_z^{1-2} - \hat{I}_z^{3-4}) - \omega_1(\sqrt{3}\hat{I}_x^{1-2} + 2\hat{I}_x^{2-3} + \sqrt{3}\hat{I}_x^{3-4}), \quad (15)$$

$$\hat{\rho}(t) = a_0\hat{1} + \sum_{i<j}\sum_{p=x,y,z} a_p^{i-j}(t)\hat{I}_p^{i-j} \quad (16)$$

where $\hat{I}_p^{i-j}$ and the commutation relationships among the $\hat{I}_p^{i-j}$ are given in Ref. [48]. The steady-state density operator is obtained by insertion of Eqs. (15) and (16) into (14), setting $\mathrm{d}\rho(t)/\mathrm{d}t = 0$, and solving for the coefficients $a_p^{i-j}(t) = a_p^{i-j}$. The change in nuclear field due to CW irradiation of the $a \to b$ transition is then computed from $\delta B_n^{a\to b} = b_n|\phi(z)|^2[Tr(\rho^{a\to b}\cdot\hat{I}_z) - Tr(\rho_0\cdot\hat{I}_z)]$. The relative change is simply

$$\frac{\delta B_n^{a\to b}}{B_n} = \frac{\langle\hat{I}_z\rangle^{a\to b} - \langle\hat{I}_z\rangle_0}{\langle\hat{I}_z\rangle_0}. \quad (17)$$

Expressions for $\delta B_n^{2\to1}/B_n$ and $\delta B_n^{3\to2}/B_n$ due to CW RF irradiation of the satellite and central transitions of an $I = \frac{3}{2}$ nucleus are provided in Appendix B. In the low power excitation regime (i.e. $T_1T_2\omega_1^2 \ll 1$), $\delta B_n^{3\to2}/\delta B_n^{2\to1} = \frac{4}{3}$. This is the same as the ratio obtained in either the low power CW excitation or FT-NMR spectrum using a hard 90° pulse. The calculations also suggest that higher power CW excitation of the central transition can completely depolarize the nuclei due to saturation of both the single quantum and triple quantum transitions, thus completely eliminating the local nuclear field of irradiated spin species.

It should be noted that δB_n is not directly detected in MDENDOR. The MDENDOR signal $\delta\Delta R_{xx}$ comes from the additional heating of the 2DES due to the increase in resonant microwave absorption. As shown in Ref. [45], for a small change, $\delta R_{xx} \propto \delta T$, where $\delta T = \bar{p}/K_{bath}$ is the increase in the electron spin temperature due to the steady-state resonant microwave power dissipation $\bar{p}$ and thermal conductance to the bath, K_{bath}. Since the ESR absorption line shape is Gaussian, the response is not linear over a wide range of δB_n values. However, for small changes, where $\delta B_n \ll \delta_{1/2}$, $\delta\bar{p} \propto \delta B_n$ and approximate linearity (i.e. $\delta R_{xx} \propto \delta B_n$) in the response can be expected.

The change $\delta B_n^{2\to1}$ due to selective excitation of the ^{75}As satellite or central transition relative to the total nuclear field can be calculated as follows. The total nuclear field includes contributions from all three isotopes:

$$B_n^{tot} = b_n^{75}\int \langle \hat{I}_z^{75}\rangle(z)\phi^2(z)\,dz + b_n^{71}\int \langle \hat{I}_z^{75}\rangle(z)\phi^2(z)\,dz + b_n^{69}\int \langle \hat{I}_z^{69}\rangle(z)\phi^2(z)\,dz. \quad (18)$$

Eq. (18) can be simplified under conditions of appreciable steady-state ESR saturation by noting that for each isotope, the steady-state Zeeman order enhancement is, according to Eq. (5), $\langle \hat{I}_z\rangle \approx -\langle \hat{I}_z\rangle_{eq} s(\gamma_e/\gamma_n)$. Thus, for $I=\frac{3}{2}$, $\langle \hat{I}_z\rangle = \frac{5}{4}\beta_{eq} s\gamma_e B_0$, demonstrating that the steady-state DNP enhanced Zeeman order does not depend on γ_n and is therefore the same for all three isotopes. As a further approximation, note that the spatial profile of the Zeeman order in the long time-scale, steady-state limit will be essentially constant within a narrow QW, since spin-diffusion will tend to equalize differences in Zeeman order on a much greater length scale. Under these conditions the steady-state spatial profile of the Zeeman order will be roughly the same for all three isotopes, yielding

$$B_n^{tot} \approx (b_n^{75} + b_n^{69} + b_n^{71})\int_{-W_e/2}^{W_e/2} \langle \hat{I}_z\rangle(z)\phi^2(z)\,dz. \quad (19)$$

Using the measured hyperfine coupling constants for this sample [9], the fractional contribution from ^{75}As is $B_n^{75}/B_n^{tot} \approx 0.5$. This would be the relative change if the nuclear spin polarization of ^{75}As were driven to zero. From Appendix B, the change in the nuclear field due to steady-state saturation of the ^{75}As satellite transition is $\delta B_n^{75,2\to1}/B_n^{75} = 1/10$, yielding

$$\frac{\delta B_n^{75,2\to1}}{B_n^{tot}} \approx 0.05. \quad (20)$$

3.3. RF swept MDENDOR

In the previous section it was demonstrated that CW NMR excitation at small B_n can facilitate sequential acquisition of individual single quantum transitions in ^{75}As without loss of the pinning condition. This provides the impetus for the development of an RF frequency swept variation of MDENDOR with the following advantages: (1) the NMR spectrum is recorded at constant Landau level filling factor and (2) efficient signal averaging is facilitated. In the frequency swept method a broad frequency range can be scanned rapidly, facilitating efficient signal averaging. In the field swept procedure, the sweep rate must be kept very low to avoid losing the pinning condition. Moreover, a lengthy recycle delay is necessary to accommodate the re-establishment of thermal equilibrium prior to repeating the field swept acquisition. The new procedure is illustrated with the aid of the experimental data presented in Fig. 6. First, the static field B_0 is ramped slow (c.a. 4.6 mT/min) down to the ESR

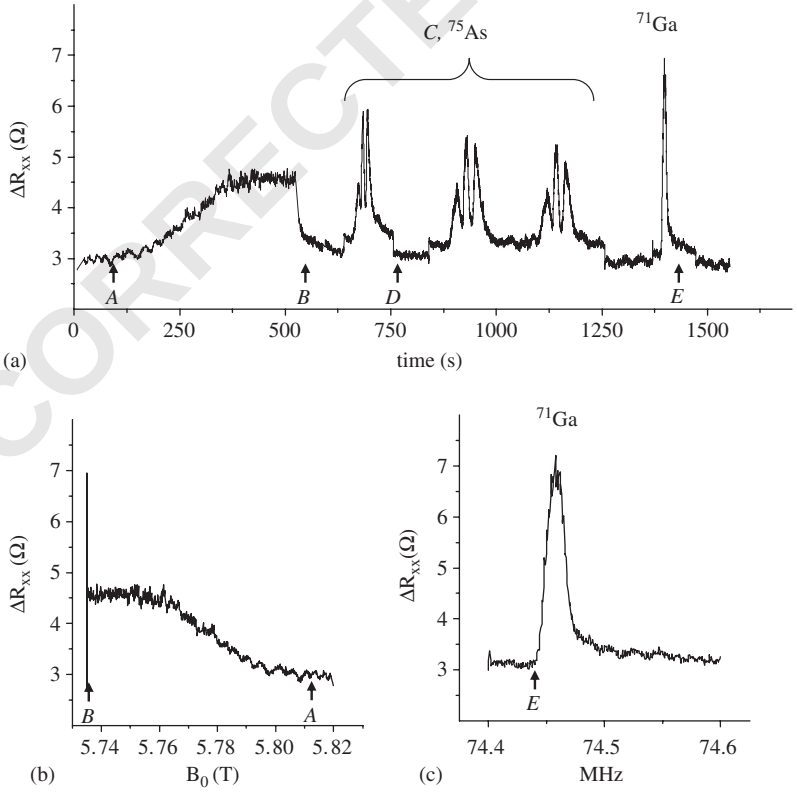

Fig. 6. The RF swept MDENDOR spectrum is acquired by a procedure illustrated by the plots of the magnetoresistance change as a function of (a) time (b) field and (c) RF frequency. The reference points $A-E$ are described in the text.

resonance, where at point "*A*" the resonant condition becomes pinned due to the onset of DNP. The down sweep is continued to a point beyond the initial resonance field and then stopped to allow a steady-state local nuclear field B_n to develop, as at point "*B*." This "stop field" is chosen such that any change δB_n due to NMR depolarization will be large enough to yield adequate signal, but small enough to avoid NMR de-pinning (i.e. $\delta B_n < \delta_{1/2}$). After reaching a steady-state, the RF frequency is swept through the NMR spectrum. Each NMR transition causes a perturbation δB_n which is registered as a change δR_{xx}. Following the passage through each NMR transition, B_n is restored by DNP and the pinning condition is re-established. The regions labeled "C" represent repeated RF sweeps through the ^{75}As spectrum. The RF field also produces a small non-resonant signal, which vanishes when the RF synthesizer is switched off, as at point "D." The RF frequency was switched at point "E" to record the ^{71}Ga transition at the same magnetic field.

Fig. 5b presents the frequency swept ^{75}As MDENDOR spectrum of sample EA124 acquired at the same microwave frequency, temperature and magnetic field, used to record the spectrum of Fig. 5a. The abscissas have been converted to ppm units to facilitate direct comparison of the spectra. The line spacing and intensity pattern are similar in the two spectra. The improved S:N of the RF swept spectrum should be noted, although this will in general vary with the choice of resonance condition for the field swept technique (see Fig. 2) or stop field initialization in the case of the RF swept spectrum. Higher S:N is also a benefit of increased resolution. The RF swept spectrum exhibits somewhat narrower resonance lines. The resolution in both the RF and field swept methods can be limited by the DNP rate following NMR perturbation of each resonance line component. This will in turn depend on experimental parameters such as the microwave field intensity, stop-field initialization condition and the Landau level filling factor. If the RF sweep rate is too high, the nuclei do not have sufficient time to repolarize following the NMR perturbation and the magnetoresistance does not return to its pre-NMR steady-state value prior to encountering subsequent NMR transitions. The natural NMR line width is expected only for sufficiently slow RF sweeps (slow passage condition).

The effect of RF field strength and magnitude of the initial steady-state nuclear field was also investigated. In Fig. 7a, the observed amplitude changes due to excitation of the satellite and central transitions are plotted as a function of the RF power. It should be noted that no effort was made to match the coil to the 50 Ω source impedance, so an accurate estimate of ω_1 is unavailable. Nevertheless, ΔR_{xx} appears to saturate with increasing RF power. Since the central-to-satellite integrated signal ratio remains close to the theoretical value of 4:3 over the entire range, the observed saturation of ΔR_{xx} probably indicates that the steady-state NMR condition $d\rho/dt = 0$ is being approached at the fixed RF sweep rate of 1 kHz/s. The

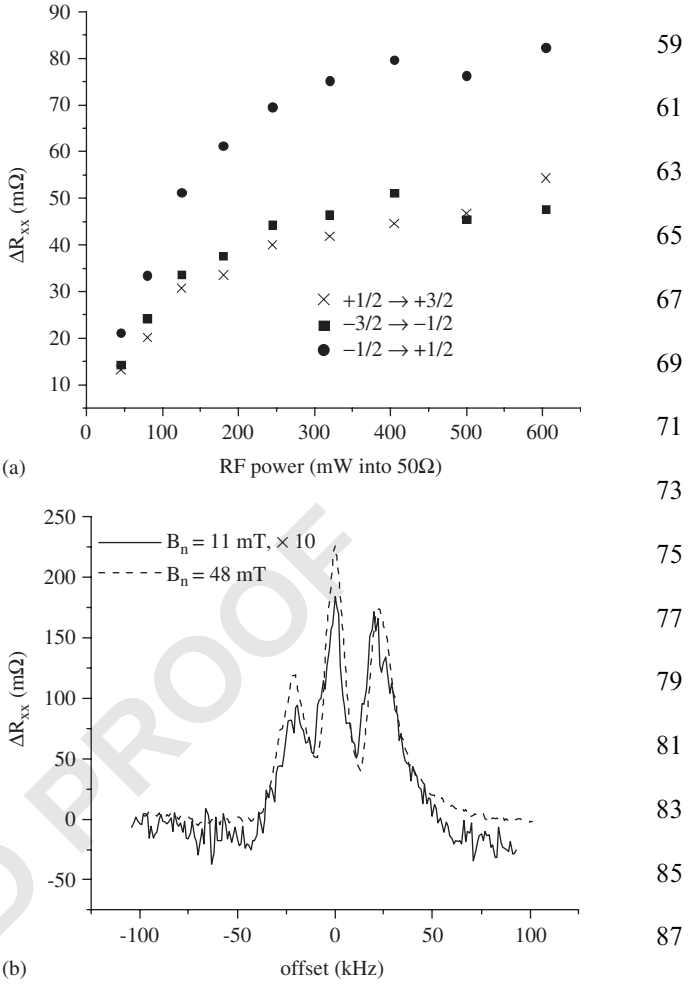

Fig. 7. (a) RF power dependence of the ^{75}As satellite and central transitions in EA124 at 1.5 K. (b) RF swept ^{75}As MDENDOR spectra acquired following a DNP down sweep at −4.6 mT/min with a microwave frequency of 32.40 GHz. The spectra were acquired at two different stop fields, 5.5355 and 5.4988 T, corresponding to local nuclear fields of approximately 11 and 47.7 mT, respectively.

observed quadrupole splitting did not vary over the range of applied RF fields tested.

The effect of varying the stop field on the observed quadrupole splitting is investigated in Fig. 7b, where representative spectra acquired at two substantially different values of the stop field, 11 and 48 mT below the thermal equilibrium ESR condition, are presented. Comparison of the two spectra shows that the same quadrupole splitting is obtained. However, the ratio of the observed ΔR_{xx} signals is about 10:1, demonstrating the advantage of acquiring the RF swept MDENDOR spectra at the highest possible nuclear field.

The dependence $\omega_Q(\theta_y)$ in EA124 on the rotation angle about the Hall bar *y*-axis is presented in Fig. 4. It obviously does not fit the $3\cos^2\theta - 1$ dependence for an EFG with $\eta = 0$ and $z \| z'$ which is typical of mounting strain. In principle, the electric quadrupole moment of nuclei near a semiconductor surface will couple to the EFG associated with band-bending. Since magnetoresistance detection is

selective to nuclei within a few magnetic lengths of the edge of the Hall bar, it is likely that band bending contributes to the observed EFG. The EFG near the edge of the Hall bar might be expected to be axially symmetric with an orientation $z' \| y$. In this case, ω_Q would remain constant with respect to rotation about θ_y. Since this is not what is observed experimentally, it must be concluded that the orientation is not $z' \| z$. The possibility that $z' \| y$ with $\eta \neq 0$ cannot be ruled out. The anisotropy is also uncertain. It should be noted that the splitting did not change when I_x was varied from 0.005 to 5 μA. Thus, the Hall potential V_{xy} does not induce an observable contribution to the splitting. There was a small but observable effect of the Landau level filling factor on ω_Q, as shown by the representative spectra shown in Fig. 8. The quadrupole splitting increased slightly with filling factor in the range $\nu = 0.978 \rightarrow 1.071$. The increase could be interpreted with the aid of Fig. 1b, which illustrates the formation of the current carrying edge states at the intersection of E_F with the lowest spin-split Landau level due to band bending. An increase in the filling factor causes this intersection to move closer to the edge where the EFG is greater, thereby increasing ω_Q.

We now demonstrate the efficiency of RF swept MDENDOR with the detection of weak NMR transitions. For example, $|\Delta m_I| = 2$ overtone transitions become weakly allowed due to state mixing by the non-secular terms $\propto \hat{I}_x^2 - \hat{I}_y^2$ of the quadrupole Hamiltonian [17,18]. Fig. 9a presents the ^{75}As overtone spectrum, obtained by averaging 4 individual RF scans at twice the ^{75}As Larmor frequency. As expected from Eq. (9), the splitting between the lines of this doublet is $2\omega_Q$, the same as the splitting between the satellite transitions of the $|\Delta m_I| = 1$ spectrum acquired at the same orientation. Signal-averaging also facilitated the observation of the overtone spectrum of ^{69}Ga, as shown in Fig. 10a, even though the quadrupole splitting is not even resolved for this nucleus. Repeated attempts to observe the overtone absorption at $3\omega_0$ were unsuccessful for all three isotopes, a result which is not surprising since there are no terms mixing the $|\pm 3/2\rangle$ states. Excitation of triple quantum coherence is possible by application of a selective pulse to the $|-1/2\rangle \rightarrow |+1/2\rangle$ transition [48].

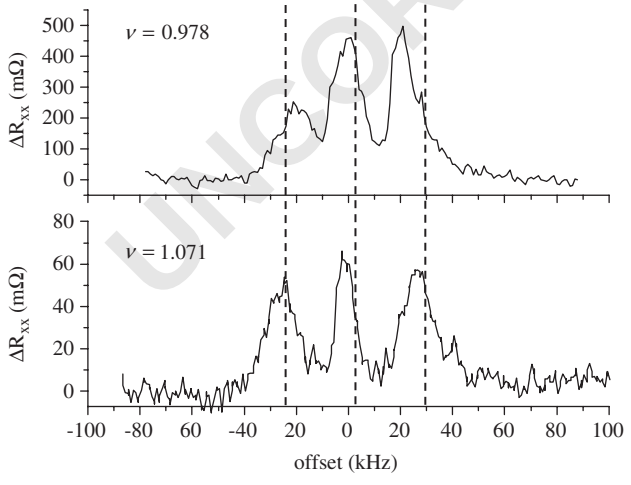

Fig. 8. Representative spectra illustrating the filling factor dependence of the ^{75}As spectrum in EA124. The RF frequency was swept at a rate of ±1 kHz/s with a frequency step size of 1 kHz.

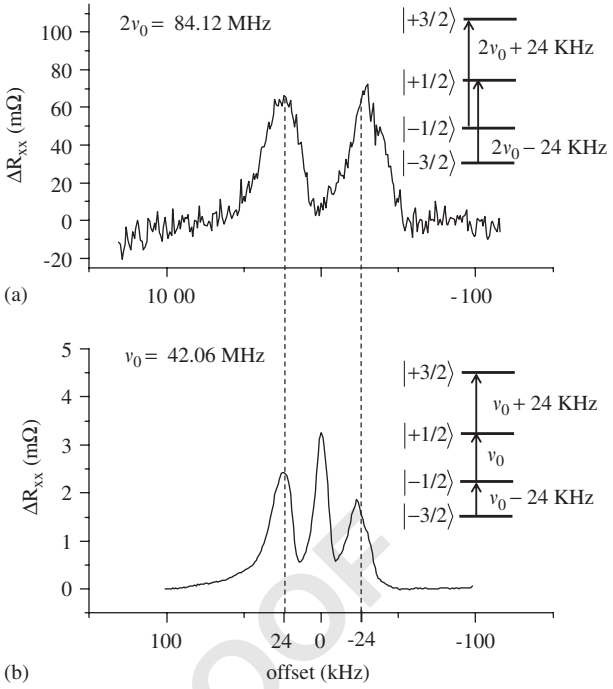

Fig. 9. (a) ^{75}As overtone spectrum ($\Delta m = 2$) observed by RF irradiation at twice the nuclear Larmor frequency. The spectrum represents the average of 4 frequency scans. (b) Single quantum ^{75}As spectrum in EA124 after averaging 4 scans, shown on the same frequency offset scale for comparison purposes. Both spectra were acquired at a tilt angle of 61° by RF swept MDENDOR at 5.772 T and 1.5 K using a microwave frequency of 34.00 GHz. The RF frequency was swept at a rate of ±1 kHz/s with a frequency step size of 1 kHz.

Finally, we present the application of RF swept MDENDOR to sample AG662, the 400 nm wide GaAs/AlAs digital PQW. In Fig. 11, the spectra of ^{71}Ga, ^{69}Ga and ^{75}As were recorded at a tilt angle of $\theta = 16°$ within the $\nu = 1$ resistance minimum. The relative signal amplitudes reflect differences in the local nuclear field associated with each isotope. The NMR line widths of the three isotopes were found to be 21, 22 and 30 kHz, respectively. The ^{75}As line in the PQW sample appears to be split, but is not quite resolved, presumably due to inhomogeneous broadening. The observation that the broadening is greatest for ^{75}As is a good indication that the line width is dominated by the distribution of strains or electric fields in the GaAs/AlAs superlattice. As shown in Fig. 12a,b, the ^{75}As line exhibits a substantial increase in broadening as the sample is rotated from $\theta_y = 0 \rightarrow 16°$. Thus, the spectrum represents a distribution of EFG's with z' not parallel to z (the growth axis). The ^{75}As spectra of EA124 acquired at two different tilt angles are plotted on the same frequency axis to facilitate a comparison of the two samples. Both the splitting and line broadening increase with increased

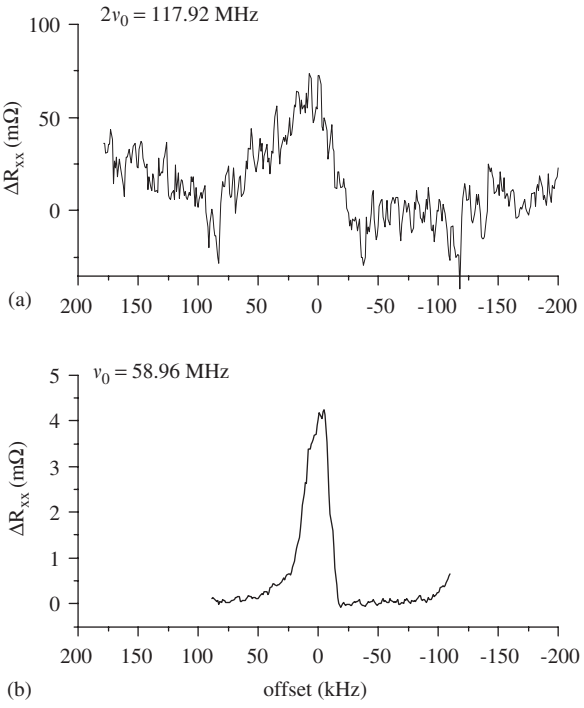

Fig. 10. (a) ^{69}Ga overtone spectrum ($\Delta m = 2$) observed by RF irradiation at twice the ^{69}Ga Larmor frequency. The spectrum represents the average of 20 frequency scans. (b) Single quantum spectrum obtained after averaging 2 scans, shown on the same frequency offset scale for comparison purposes. Both spectra were acquired at a tilt angle of 61° by RF swept MDENDOR at 5.772 T and 1.5 K using a microwave frequency of 34.00 GHz. The RF frequency was swept at a rate of ±1 kHz/s with a frequency step size of 1 kHz.

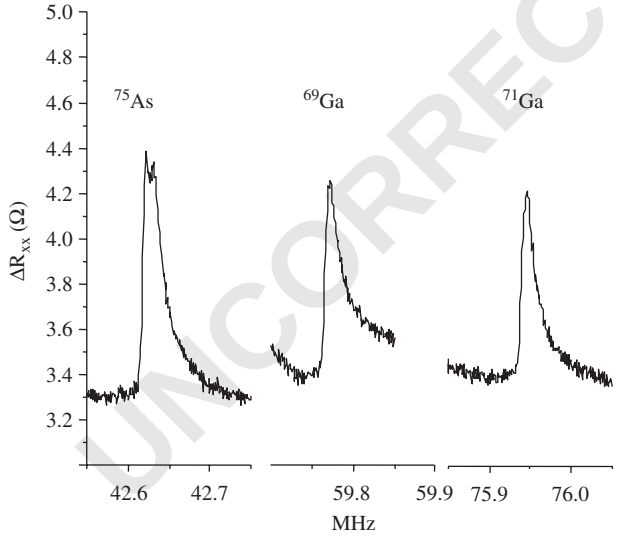

Fig. 11. RF swept MDENDOR transitions observed at filling factor $\nu = 1$ in the 400 nm wide GaAs/AlAs digital parabolic QW sample (AG662) by CW microwave excitation of ESR at a steady-state nuclear field of 38 mT while sweeping the RF field at a rate of ±1 kHz/s with a frequency step size of 1 kHz. No signal due to ^{27}Al transitions could be observed, even after averaging 16 frequency scans.

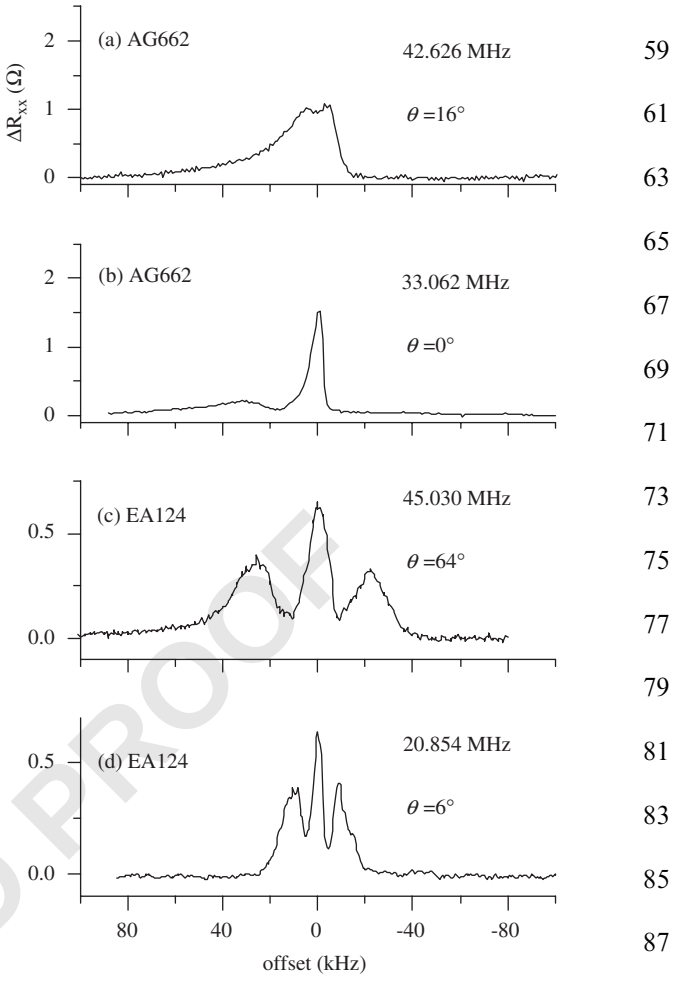

Fig. 12. Comparison of the RF swept MDENDOR spectra acquired on the two different QW samples, each at two different tilt angles. All spectra were recorded at approximately 1.5 K.

rotation angle. Furthermore, the central transition is narrower than the satellite transitions due to the fact that the former is unaffected by the quadrupole interaction to first order. A comparison of the spectra of EA124 and AG662 reveals that the strain field is more homogeneous in the narrow QW sample.

It should be possible to observe an ^{27}Al NMR signal if the subband wavefunction $\phi(z)$ extends appreciably into the AlAs layers of the PQW. In principle, the relative amplitude of the ^{27}Al signal could be used to evaluate the extent of the electronic delocalization in the quantum structure. However, repeated attempts to observe a ^{27}Al NMR signal were unsuccessful, even after averaging the signals of 16 frequency scans, despite the >25:1 S/N ratio obtained on the other three isotopes after only a single scan.

3.4. Conclusions

DNP enhancement of the local nuclear field can be exploited for the detection of NMR in the vicinity of a

2DES at odd integer filling factors in the integer QHE. In the foregoing we have developed a quantitative model to account for the MDENDOR signals obtained in these systems under a variety of experimental conditions. The model incorporates the effects of DNP, magnetic field pinning of the ESR, nuclear spin-diffusion and NMR depolarization. Numerical simulations based on this model successfully reproduced the dependence of the magnetoresistance response on the initial local nuclear field. The simulations confirm the simple physical interpretation of the signals in terms of a disruption of the steady-state pinning condition. The model also provided the impetus for the proposal of a new RF swept variation of the MDENDOR. The novel RF swept method affords more efficient signal averaging and the ability to perform NMR experiments at a fixed static field where the filling factor is constant and well defined. The RF swept technique is therefore advantageous for spectroscopic investigation of the highly correlated electron states associated with the QHE.

The splitting of the ^{75}As MDENDOR resonance in EA124 (30 nm wide GaAs QW) indicates a homogeneous electric-quadrupole interaction in this sample. Expression of the local nuclear field in the fictitious spin-1/2 operator basis permitted the calculation of the change in the nuclear field due to selective CW-NMR irradiation of individual satellite and central transitions. The calculation reveals that low power selective irradiation of the central transition produces a $\frac{4}{3}$ greater change in the nuclear field then irradiation of the satellite transition. The calculations also suggests that higher power CW excitation of the central transition can completely depolarize the nuclei due to saturation of both the single quantum and triple quantum transitions, thus completely eliminating the local nuclear field of irradiated spin species. Removal of the nuclear field by this technique could lead to increased electron spin coherence times.

The utility of RF-swept MDENDOR has been demonstrated with the observation of weakly allowed overtone transitions of nuclei situated in the conduction channel and characterization of electric quadrupole interactions in two types of QW structures. The overtone data, together with the rotation angle dependences, indicate that the z' principle axis of the EFG does not lie along the growth axis, as is the case in a sample subjected to a planar stress. This finding, together with the fact that the spin currents are carried by edge states within a few magnetic lengths of the edge of the Hall bar mesa, suggests that the observed EFG probably includes a contribution from band bending. The observed rotation dependence could be explained if z' is oriented roughly along the Hall bar y-axis with $\eta \neq 0$. Future experimental work will entail a rotation study about the x as well as the y-axis. Finally, we note that it should be possible to observe an ^{27}Al NMR signal if the subband wave function extends appreciably into the Al containing regions away from the centre of the PQW. In principle, the relative amplitude of the ^{27}Al signal could be used to evaluate the extent of the electronic delocalization. However, the inability to detect any signal indicates that the spin currents do not extend appreciably into the AlAs layers of the digital superlattice. This finding is consistent with recent measurements of the g-factor and its anisotropy in this same sample [14].

Acknowledgments

We would like to thank Greg Labbe and John Graham of the UF Physics Department for technical support. This work was supported by NSF Grant DMR-0106058, CNP/q-NSF US-Brazil Cooperative Research Grant 0334573, and the University of Florida. Provision of the digital parabolic QW sample by A.I. Toropov and A.K. Bakarov of the Institute of Semiconductor Physics, Novosibirsk, Russia, is gratefully acknowledged.

Appendix A. Derivation of a difference equation for spin diffusion

A difference equation for the spin diffusion term, $D^i\partial^2\langle\hat{I}_z^i\rangle/\partial z^2$, is derived as follows. The total z-angular momentum of N_j nuclei in atomic layer j of volume $V_j = Aa_0$ is $\langle I_{zj}\rangle\rho$, where $\rho = N_j/V_j$. Letting $J^{i,j}$ denote the flux of the total angular momentum per unit area per unit time from layer $j-1$ into layer j, Fick's Law can be introduced:

$$J^{i,j} = -D^i\frac{\mathrm{d}[\rho\langle I_z^{i,j}\rangle]}{\mathrm{d}z} = -D\frac{(\langle I_z^{i,j}\rangle - \langle I_z^{i,j-1}\rangle)\rho}{a_0}. \tag{21}$$

Similarly, the flux from layer j to layer $j+1$ is $J^{i,j+1} = D(\langle I_z^{i,j}\rangle - \langle I_z^{i,j+1}\rangle)\rho/a_0$.Since the density of the material is constant, the net flux of spin angular momentum obeys

$$\frac{\mathrm{d}\langle I_z^{i,j}\rangle}{\mathrm{d}t} = \frac{D^i}{a_0^2}(\langle I_z^{i,j-1}\rangle + \langle I_z^{i,j+1}\rangle - 2\langle I_z^{i,j}\rangle). \tag{22}$$

For a small enough time increment, Δt, it is valid to use

$$\Delta\langle I_z^{i,j}\rangle = \frac{D^i}{a_0^2}(\langle I_z^{i,j-1}\rangle + \langle I_z^{i,j+1}\rangle - 2\langle I_z^{i,j}\rangle)\Delta t \tag{23}$$

provided that the stability criterion [49] $2D^i\Delta t \ll a_0^2$ is met.

Appendix B. Analysis of the nuclear field for Spin-3/2

Satellite transition: $|1/2\rangle \rightarrow |3/2\rangle$

The rotating frame Hamiltonian describing the selective irradiation of the $|+1/2\rangle \rightarrow |+3/2\rangle$ transition is obtained by setting $\Delta\omega \rightarrow \omega_Q$ in Eq. (15)

$$\hat{H} = -2\omega_Q(\hat{I}_z^{1-4} + \hat{I}_z^{2-4}) - \omega_1(\sqrt{3}\hat{I}_x^{1-2} + 2\hat{I}_x^{2-3} + \sqrt{3}\hat{I}_x^{3-4}), \tag{24}$$

$$\approx -2\omega_Q(\hat{I}_z^{1-4} + \hat{I}_z^{2-4}) - \sqrt{3}\omega_1\hat{I}_x^{1-2}. \tag{25}$$

The last two terms are truncated if $\omega_Q \gg \omega_1$ and can be neglected in this limit. Insertion of 25 into 14 with

$d\rho(t)/dt = 0$ yields:

$$a_0 = \tfrac{1}{4}, \tag{26a}$$

$$a_z^{1-2} = a_z^{2-3} + a_z^{2-4} - \frac{1}{4}\beta_0\omega_0\frac{1+6T_1T_2\omega_1^2}{1+3T_1T_2\omega_1^2}, \tag{26b}$$

$$a_z^{1-3} = -a_z^{1-4} - a_z^{2-3} - a_z^{2-4} + \beta_0\omega_0, \tag{26c}$$

$$a_z^{3-4} = -a_z^{1-4} - a_z^{2-4} + \tfrac{3}{4}\beta_0\omega_0, \tag{26d}$$

$$a_y^{1-2} = \frac{\sqrt{3}}{4}\beta_0\omega_0\frac{T_2\omega_1}{1+3T_1T_2\omega_1^2}. \tag{26e}$$

From the density operator, reconstructed from Eq. (16), yielding

$$\frac{\delta B_n^{2\to1}}{B_n} = \frac{3T_1T_2\omega_1^2}{10+30T_1T_2\omega_1^2}. \tag{27}$$

Incidentally, the single quantum coherence NMR signal due to irradiation of the satellite is

$$S^{2\to1} = Tr(\rho^{2\to1}\hat{I}_y) = \frac{3}{8}\beta_0\omega_0\frac{T_2\omega_1}{1+3T_1T_2\omega_1^2}. \tag{28}$$

Central transition: $|-1/2\rangle \to |+1/2\rangle$

The rotating frame Hamiltonian describing the selective irradiation of the $|-1/2\rangle \to |+1/2\rangle$ transition is obtained by setting $\Delta\omega \to 0$ in Eq. (15), yielding

$$\hat{H} = \omega_Q(\hat{I}_z^{1-2} - \hat{I}_z^{3-4}) - \omega_1(\sqrt{3}\hat{I}_x^{1-2} + 2\hat{I}_x^{2-3} + \sqrt{3}\hat{I}_x^{3-4}). \tag{29}$$

For irradiation of the central transition, the unitary transformation $U_y^{1-2}(-\theta)U_y^{3-4}(\theta)$, where $\theta = \tan^{-1}(\sqrt{3}\omega_1/\omega_Q)$, of the Hamiltonian and initial density matrix facilitates derivation of analytical solutions for the NMR observables. In the $\omega_1 \ll \omega_Q$ regime,

$$\hat{H}_T \simeq \omega_Q(\hat{I}_z^{1-2} - \hat{I}_z^{3-4}) - 2\omega_1\hat{I}_x^{2-3} - \frac{3}{2}\left(\frac{\omega_1^3}{\omega_Q^2}\right)\hat{I}_x^{1-4}. \tag{30}$$

In the same approximation, $\rho_{T,0} \simeq \rho_0$, and $\hat{I}_{T,x} \simeq \hat{I}_x$, $\hat{I}_{T,y} \simeq \hat{I}_y$, and $\hat{I}_{T,z} \simeq \hat{I}_z$, yielding

$$0 = -i[H_T, \rho_T] - \frac{\rho_{T,off}}{T_2} - \frac{\rho_{T,diag} - \rho_{T,0}}{T_1}. \tag{31}$$

Eq. (31) reduces to

$$a_0 = \tfrac{1}{4}, \tag{32a}$$

$$a_z^{12} = -a_z^{13} + a_z^{24} + a_z^{34}, \tag{32b}$$

$$a_z^{14} = -a_z^{24} - a_z^{34} + \frac{3\beta_0\omega_0\omega_Q^4}{9T_1T_2\omega_1^6 + 4\omega_Q^4}, \tag{32c}$$

$$a_z^{23} = -a_z^{13} + a_z^{34} + \frac{1}{4}\beta_0\omega_0\frac{1}{1+4T_1T_2\omega_1^2}, \tag{32d}$$

$$a_y^{14} = \frac{1}{2}\beta_0\omega_0\frac{9T_2\omega_1^3\omega_1^2}{9T_1T_2\omega_1^6 + 4\omega_Q^4}, \tag{32e}$$

$$a_y^{23} = \frac{1}{2}\beta_0\omega_0\frac{T_2\omega_1}{1+4T_1T_2\omega_1^2}. \tag{32f}$$

Substitution of the coefficients into Eq. (16) and evaluation of the trace yields:

$$Tr[\rho^{3\to2}\hat{I}_z] = \frac{1}{2}\beta_0\omega_0\left(\frac{1}{4+16T_1T_2\omega_1^2} + \frac{9\omega_Q^4}{9T_1T_2\omega_1^6 + 4\omega_Q^4}\right). \tag{33}$$

Thus,

$$\frac{\delta B_n^{3\to2}}{B_n} = 1 - \frac{1}{10+40T_1T_2\omega_1^2} - \frac{18\omega_Q^4}{5(9T_1T_2\omega_1^6 + 4\omega_Q^4)}. \tag{34}$$

Finally, the single quantum CW-NMR signal would be

$$S^{3\to2} = Tr(\rho^{3\to2}\hat{I}_y) = \frac{1}{2}\beta_0\omega_0\frac{T_2\omega_1}{1+4T_1T_2\omega_1^2} \tag{35}$$

Thus, we obtain the usual ratio of the single quantum signals

$$\frac{S^{2\to3}}{S^{1\to2}} = \frac{4}{3}\left(\frac{1+3T_1T_2\omega_1^2}{1+4T_1T_2\omega_1^2}\right), \tag{36}$$

where in the low power regime, we get the usual 4:3 ratio of the central:satellite signal amplitudes. This can be compared to the ratio of the change in the nuclear field for irradiation of these transitions

$$\frac{\delta B_n^{2\to3}}{\delta B_n^{1\to2}} = \frac{1}{3}\frac{(1+3T_1T_2\omega_1^2)(9\omega_1^4(9+40T_1T_2\omega_1^2) + 16\omega_Q^4)}{(1+4T_1T_2\omega_1^2)(9T_1T_2\omega_1^6 + 4\omega_Q^4)}. \tag{37}$$

It is interesting to evaluate this expression in various RF excitation power regimes:

Case 1: low power, $\omega_1 \to 0$: $(\delta B_n^{2\to3}/\delta B_n^{1\to2}) = \frac{4}{3}$.

Case 2: saturation of 1QC but not 3QC : $(\delta B_n^{2\to3}/\delta B_n^{1\to2}) = 1$.

Case 3: saturation of 1QC and 3QC, but $\omega_Q \gg \omega_1$: $(\delta B_n^{2\to3}/\delta B_n^{1\to2}) = 10$.

References

[1] F. Meier, B.P. Zakharchenya (Eds.), Optical Orientation, North-Holland, New York, 1984.
[2] J.-M. Spaeth, H. Overhof, Point Defects in Semiconductors and Insulators, Springer, Heidelberg, 2003 Chapter 8.
[3] M.J. Snelling, et al., Phys. Rev. B 44 (1991) 11345–11352.
[4] M. Schreiner, H. Hochstetter, H. Pascher, S.A. Studenikin, J. Mater. Res. 124 (1997) 80.
[5] M. Schreiner, et al., Solid State Commun. 102 (1997) 715.
[6] M. Eickhoff, B. Lenzmann, G. Flinn, D. Suter, Phys. Rev. B 65 (2002) 125301.
[7] Eickhoff, et al., Phys. Rev. B 67 (2003) 085308.

[8] J.G. Kempf, D.P. Weitekamp, J. Vac. Sci Technol. B 18 (2000) 2255–2262.
[9] S.A. Vitkalov, C.R. Bowers, J.L. Reno, J.A. Simmons, Phys. Rev. B 61 (2000) 5447.
[10] W. Desrat, et al., Phys. Rev. Lett. 88 (2002) 256807.
[11] Ivchenko, et al., Sov. Phys. Semicond. 26 (1992) 827.
[12] Le Jeune, et al., Semicond. Sci. Technol. 12 (1997) 380.
[13] M. Dobers, K.v. Klitzing, G. Weimann, Solid State Commun. 70 (1989) 41–44.
[14] J.D. Caldwell, C.R. Bowers, G. Gusev, Phys. Rev. B. (2005), in press.
[15] A. Berg, et al., Phys. Rev. Lett. 64 (1990) 2563.
[16] N.N. Kuzma, et al., Science 281 (1998) 686.
[17] C.P. Slichter, Principles of Magnetic Resonance, Spring, New York, 1990.
[18] A. Abragam, Principles of Nuclear Magnetism, Oxford University Press, Oxford, 1985, pp. 364–370.
[19] S.K. Buratto, D.N. Shykind, D.P. Weitekamp, J. Vac. Sci. Technol. B 10 (1992) 1740.
[20] J.P. Marohn, et al., Phys. Rev. Lett. 75 (1995) 1364–1367.
[21] R. Meisels, Semicond. Sci. Technol. 20 (2005) R1–R18.
[22] S.E. Barrett, et al., Phys. Rev. Lett. 74 (1995) 5112.
[23] P. Khandelwal, et al., Physica B 256 (1998) 113.
[24] R. Tycko, et al., Science 268 (1995) 1460.
[25] G. Gervais, et al., Phys. Rev. Lett. 94 (2005) 196803.
[26] J. Stolze, D. Suter, Quantum Computing: A Short Course from Theory to Experiment, Wiley-VCH, Berlin, 2004.
[27] M. Mehring, Appl. Magn. Reson. 17 (1999) 141.
[28] E. Hahn, Phys. Rev. 80 (1950) 580.
[29] E.R. Andrew, A. Bradbury, R.G. Eades, Nature 182 (1958) 1659; E.R. Andrew, A. Bradbury, R.G. Eades, Nature 183 (1958) 1802.
[30] J.S. Waugh, L.M. Huber, U. Haeberlen, Phys. Rev. 20 (1968) 180.
[31] R.R. Ernst, G. Bodenhausen, A. Wokaun, Principles of Nuclear Magnetic Resonance in One and Two Dimensions, Clarendon Press, Oxford, 1987.
[32] R. Freeman, Spin Choreography. Basic Steps in High Resolution NMR, Spektrum, Oxford, 1997.
[33] M. Mehring, W. Scherer, A. Weidinger, Phys. Rev. Lett. 93 (2004) 206603 See and references within.
[34] H.-W. Jiang, E. Yablonovitch, Phys. Rev. B 64 (2001) 041307.
[35] G. Salis, et al., Nature 414 (2001) 619.
[36] S.A. Vitkalov, C.R. Bowers, J.A. Simmons, J.L. Reno, J. Phys. Condens. Mater. 11 (1999) L407.
[37] P. Streda, J. Kucera, A.H. MacDonald, Phys. Rev. Lett. 59 (1987) 1973.
[38] J.D.F. Franklin, et al., Physica B 249 (1998) 405.
[39] M. Dobers, et al., Phys. Rev. Lett. 61 (1988) 1650–1653.
[40] C. Hillman, H.W. Jiang, Phys. Rev. B 64 (2001) 201308.
[41] E. Olshanetsky, et al., Physica B (2005), in press.
[42] A. Usher, R.J. Nicholas, J.J. Harris, C.T. Foxon, Phys. Rev. B 41 (1990) 1129.
[43] A. Schmeller, et al., Phys. Rev. Lett. 75 (1995) 4290.
[44] K.V. Klitzing, G. Dorda, M. Pepper, Phys. Rev. Lett. 45 (1980) 494.
[45] E. Olshanetsky, et al., Phys. Rev. B 67 (2003) 165325.
[46] C.S. Sergio, et al., Phys. Rev. B. 64 (2001) 115314.
[47] S. Vega, A. Pines, J. Chem. Phys. 66 (1977) 5624.
[48] S. Vega, J. Chem. Phys. 68 (1978) 5518.
[49] W.H. Press, S.A. Teukolsky, W.T. Vetterling, B.P. Flannery (Eds.), Numerical Recipes C, second Ed., 1992. Cambridge.